Applied Surface Science 520 (2020) 146328

Contents lists available at ScienceDirect

Applied Surface Science

journal homepage: www.elsevier.com/locate/apsusc

Femtosecond laser fabrication of LIPSS-based waveplates on metallic surfaces

A. San-Blas[a,b,*], M. Martinez-Calderon[a,b,1], J. Buencuerpo[c,2], L.M. Sanchez-Brea[c], J. del Hoyo[c], M. Gómez-Aranzadi[a,b], A. Rodríguez[a,b], S.M. Olaizola[a,b]

[a] Ceit, Manuel Lardizabal 15, 20018 Donostia/San Sebastián, Spain
[b] Universidad de Navarra, Tecnun, Manuel Lardizabal 13, 20018 Donostia/San Sebastián, Spain
[c] Applied Optics Complutense Group, Optics Department, Universidad Complutense de Madrid, Facultad de Ciencias Físicas, Ciudad Universitaria s.n., 28040 Madrid, Spain

ARTICLE INFO

Keywords:
LIPSS
Laser
Femtosecond
Nanostructure
Polarization
Waveplate

ABSTRACT

A fast and reliable method for the fabrication of polarization modifying devices using femtosecond laser is reported. A setup based on line focusing is used for the generation of LIPSS on stainless steel, processing at different speeds between 0.8 and 2.4 mm/s with constant energy per pulse of 1.4 mJ. SEM and AFM characterizations of the LIPSS show a progressive increase in period as the processing speed increases, while height remains approximately constant in the studied range. Optical characterization of the devices shows an induced change in the polarization of the reflected beam that varies with the processing speed, which allows a controlled fabrication of these devices.

1. Introduction

Converting the state of polarization of a laser beam is an essential task in most optical research and industrial applications [1]. For this purpose, waveplates are one of the most common elements in present-day optical setups.

Conventional waveplates manipulate the polarization state by retarding (or delaying) one of the polarization components with respect to its orthogonal component. This behavior is achieved through different phenomena, namely, birefringence (inducing a progressive delay as the wave travels through a material) and internal total reflection (as in Fresnel rhombs, which take advantage of the induced phase shifts between the polarization components in each internal reflection [2]). Either of this phenomena can happen naturally in transparent materials (crystals) or be mechanically induced (fibers) [3,4].

For this reason, most waveplates are nowadays fabricated for operating in transmissive mode. However, the rapidly growing development of nanostructuring technologies and metallic metamaterials [5] has opened interesting alternatives for the fabrication of this type of devices that operate in reflective mode [6].

Operating in reflective mode may be beneficial to certain optical systems due to physical restrictions in the setup. However, the main advantage lays in that they generally present a higher damage threshold and produce a lower temporal dispersion of the pulse [7], along with having lower heat dissipation coefficient than transmissive waveplates [8]. Some applications that use polarization and have already benefited from reflective mode are liquid-crystal displays [8], element compactation of optical pickup units [9] or devices with antireflective functionality [10].

The physical principle that allows this phase-shifting behavior in nanostructured surfaces is based on the interaction of light with subwavelength patterns/gratings (SWGs). When the period of the grating is smaller than the wavelength of the incident light, the structure becomes an optically anisotropic medium which induces optical birefringence, usually called form birefringence [11,12]. This phenomenon originates from the difference in boundary conditions of parallel and perpendicular components of the electromagnetic waves relative to the direction of the grating lines [13].

Form birefringence is very strong compared with natural anisotropic crystals, and it can be tuned by controlling the period and aspect ratio of the grating structure. This way, a SWG with properly chosen morphological parameters may operate as a half- or quarter-waveplate [14,15]. In cases like this in which SWGs are used to change and control polarization, they receive the denomination of polarization gratings (PGs).

* Corresponding author at: Ceit, Manuel Lardizabal 15, 20018 Donostia/San Sebastián, Spain.
E-mail address: asanblas@ceit.es (A. San-Blas).
[1] Present address: Auckland University, New Zealand.
[2] Present address: National Renewable Energy Laboratory, Golden, CO, USA.

https://doi.org/10.1016/j.apsusc.2020.146328
Received 29 January 2020; Received in revised form 27 March 2020; Accepted 13 April 2020
Available online 18 April 2020

Recently, many works based on this surface sub-wavelength structuring approach have been published. For example, Gadyani et al. [16] fabricated a subwavelength metal grating for visible light by electron-beam lithography to transform circularly polarized light into radially polarized light. Nanfang Yu et al. [17] achieved polarization manipulation using carefully designed antennae that create an abrupt phase change at the interface. Stafeev et al. [18] fabricated a four-Sector transmission Polarization Converter (4-SPC) for a wavelength of 633 nm, that enables the conversion of a linearly polarized incident beam into a mixture of linearly and azimuthally polarized beam.

In most of these works, the surface nanostructuring process was carried out with different variants of lithography: focused-ion-beam lithography, electron beam lithography, nanoimprint lithography or optical interference lithography [6,9,11,14,15,19]. However, these methods usually involve several fabrication steps, leading to complex and long fabrication processes. Additionally, some of them involve the use of chemicals like chrome, acids or organic resins that are potentially pollutants or health hazards.

Other methods available to create micro- or nanogratings while avoiding these shortcomings are Direct Laser Ablation (DLA) and Direct Laser Interference Patterning (DLIP). DLA consists in removing material through laser ablation, with the size of the focused spot limited by the diffraction limit, which is related to the laser wavelength and numerical aperture (NA) of the focusing system. In practice, this means that it is usually not possible to obtain spots smaller than 1 μm in the target surface. Only by using UV lasers with high NA or/and photosensitive materials, usually polymers, it is possible to achieve smaller spot sizes [20]. Naturally, this technique covers a very small surface for each irradiation, which greatly increases processing time.

DLIP is a method that uses interference between two or more coherent beams. This interference generates an intensity pattern of local maxima and minima. In the case of two beams, the generated pattern is formed by parallel lines, with the period of the structures depending on the wavelength of the laser and the angle between the interfering beams [21]. This method overcomes some of the drawbacks of DLA since a large area can be processed at the same time, in the order of 1 cm^2 versus the previously mentioned 1 μm^2. However, it requires lasers with pulses in the order of picoseconds-nanoseconds due to the need of a larger spatial coherence that makes the interference possible over regions of relevant sizes. This means that thermal effects become significant compared to femtosecond lasers, which is a critical effect when processing materials (specifically metals due to their higher thermal conductivity), therefore limiting the resolution of the pattern in practice [22].

To sum up, even though these laser techniques surmount some of the disadvantages present in lithography, they still have some limitations regarding the equipment needed to generate sub-micrometer gratings. These limitations are mainly related to the laser source (pulse duration, wavelength) and target material, being much less efficient on metals than on polymers.

In this work, we have chosen a different approach for the fabrication of this type of gratings, which consists in the use of the so-called Laser-Induced Periodic Surface Structures (LIPSS). LIPSS were discovered in 1965 [23], but they have started to receive increased attention only recently. This is due to the fast development of laser systems and sources, specially femtosecond sources, that have enabled them to become an interesting alternative for subwavelength structuring of most materials with an easy and single-step fabrication process [24].

LIPSS are periodic structures that appear easily in most materials (metals, dielectrics, and polymers) when irradiated with linearly polarized radiation [24–26]. The orientation of these structures is directly related to the polarization of the incident light, while other parameters of their morphology such as the period and height can be controlled with the number of pulses, fluence, wavelength, angle of incidence and pulse duration of the incident light [27]. Two main types of LIPSS can be generally described according to their period. Low Spatial Frequency LIPSS (LSFL) have a period close to the irradiation wavelength λ (usually between λ/2 and λ), while High Spatial Frequency LIPSS (HSFL) exhibit shorter periods (smaller than λ/2) [24]. In any case, LIPSS period is always shorter than the wavelength of the laser used in their generation. This makes simpler the fabrication of nanogratings with the use of conventional lasers emitting in the near infrared. Additionally, this method is not limited by the spot size or the type of material processed. These characteristics indicate that the generation of LIPSS for the fabrication of SWG is a very promising method that can surpass others in efficiency, versatility and speed.

In order to boost performance and fabrication speed, laser setups taking advantage of beam shaping techniques have been recently used (Bessel beams, cylindrical lens, and spatial light modulators), demonstrating that the coherence and fabrication speed can be improved this way [28–30]. In this work, we have explored the use of a focusing system employing a cylindrical lens to minimize the fabrication time and make this approach an industrially feasible alternative in terms of production rates.

Therefore, we present a new approach for the fabrication of PGs based on LIPSS. A Ti:Sapphire femtosecond laser with a cylindrical focusing system has been used to rapidly generate LSFL with different parameters on the surface of steel samples. Results confirm polarization changes in the reflected light, which are associated with the form birefringent behavior of the fabricated PGs through numerical calculations. It has been proved that the amount of change induced in the polarization can be controlled by the parameters used in the fabrication process of the samples. We believe that this method could overcome the drawbacks of fabricating waveplates with other methods by allowing a fast, versatile and controlled fabrication without the use of polluting chemicals.

2. Materials & methods

2.1. Material

The irradiated material is stainless steel (AISI 304) in samples of dimensions 10 mm × 20 mm. The raw samples were mechanically polished to finally obtain samples with a measured roughness of R_a = 276.3 Å. Before and after the process the samples were introduced in acetone ultrasound bath for 3 min in order to remove dirt and particles generated during the process.

2.2. Laser setup

A Ti:Sapphire laser is focused in a line on the surface of the stainless steel samples in order to create LIPSS along said line. The laser system produces 120 fs pulses with a central wavelength of 800 nm and a repetition rate of 1 kHz. The pulse energy is adjusted with a variable attenuator formed by a half-wave plate and a polarizer. A motorized half-wave plate rotates the polarization of the laser beam. A combination of a cylindrical lens with a 100 mm focal length and a spherical focusing lens with a 75 mm focal length is used to focus the beam on the sample with a line-shaped profile perpendicular to the X-axis (Fig. 1). This, in contrast to other reported experiments [29,31,32], allows the introduction of an imaging system to monitor the process while maintaining the line profile (with a gaussian distribution in both focused and free-propagating axes) of the focused beam. The position of the lenses is adjusted so that the distance between them is equal to the sum of their focal lengths. The imaging system is constituted by a CMOS camera using a white LED as illumination, as shown in Fig. 1. XZ motorized stages are used to hold the sample and to control the projected line size (by adjusting the Z position) and the processing speed in the X direction.

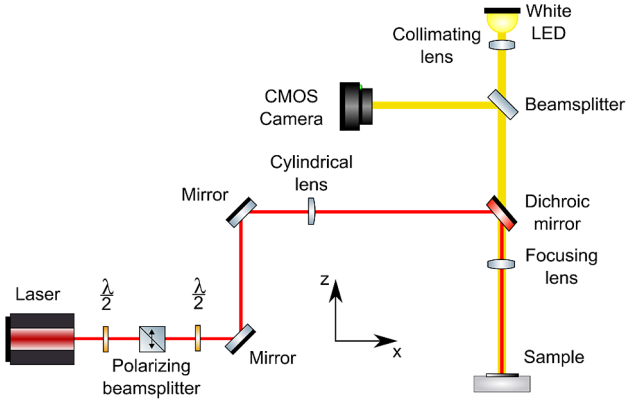

Fig. 1. Setup used in the processing of the samples.

2.3. LIPSS fabrication process

LIPSS patterns were generated moving the sample under the line-focused laser beam at a constant speed along the X-axis, with laser polarization parallel to the direction of the movement. The incoming laser beam was directed to the cylindrical lens and the position of the samples in the Z-axis (vertical) was adjusted so that the width of the laser beam projected onto their surface was constant in all cases. The beam size in the position of the sample was measured at low energy per pulse with a calibrated CCD, finding a beam half-width at e^{-2} of $w_y = 6$ mm in the non-focused axis and $w_x = 32$ μm in the focused axis.

In this case, due to the focusing of the beam, the beam area has an elliptical shape instead of a circular one, with one of the axis being much larger than the other. In consequence, fluence was calculated using the expression $F = E/(\pi \cdot w_x \cdot w_y)$, where E is the measured energy per pulse. Since the laser irradiation is non-static, an overlap exists between the pulses. In order to calculate this overlap, we consider the size of the beam width ($2 \cdot w_x$). The time required for a point in the sample to travel this distance at speed v is $2 \cdot w_x / v$. Therefore, the number of pulses to which this point is exposed during this time is $N = 2 \cdot w_x \cdot R_R / v$, where R_R is repetition rate of the laser.

A study was performed in order to select the correct parameters for LIPSS formation. Then, the energy per pulse for all the samples was set to 1.4 mJ (value measured before the focusing lenses). The range of processing speeds varied between 0.8 and 2.4 mm/s. Using these parameters resulted in a fluence of 0.2 J/cm^2 and number of pulses between 80 and 240 for the highest and lowest speed, respectively.

With the mentioned parameters and within this range of speeds, LIPSS are clearly visible in 3 mm around the center of the generated line (at the point of maximum intensity). Ablation starts to dominate the process below the minimum speed and above the maximum speed the formation of LIPSS stops. These results are in good agreement with previous studies on stainless steel [33].

2.4. Characterization

Two types of characterization were used in this study. Firstly, the morphology of the samples was examined in order to evaluate the formation and characteristics of the generated nanostructures. Secondly, an optical characterization was made in order to observe the optical response of the fabricated samples. In all cases, the characterization took place in the region around the middle of the sample where LIPSS characteristics were constant.

2.4.1. Morphological characterization

The changes on the surface of the samples were characterized with SEM (Scanning Electron Microscopy), gathering micrographs of the samples which then were analyzed through 2D-FFT (two-dimensional Fast Fourier Transform). Since the relation between LIPSS period (Λ) and the distance between FFT peaks (d) is given by equation $\Lambda = 2/d$, the period of the generated LIPSS can be measured.

Height measurements were taken with AFM (Atomic Force Microscope) in large areas of 30 μm × 30 μm using high aspect ratio tips. Each measurement consisted of 1890 linear sweeps with a separation of 16 nm between each other. The direction of the sweeps was perpendicular to the LIPSS. Then, in each sweep, all peak to valley heights were calculated and stored. These values were then collected for the total number of sweeps and represented as a histogram. The lowest peak to valley heights (with a prominence smaller than 30 nm) were filtered, since they are associated to background noise and instrumental errors. The resulting histogram was fitted to a normal distribution, from which the mean LIPSS height and standard deviation was obtained.

The transversal profile of the LIPSS was also observed through the FIB (Focused Ion Beam) technique implemented in a SEM microscope. This technique is useful to compare the obtained data with the results from the AFM, although the process is time consuming and, in consequence, it is difficult to obtain significant statistical data with it.

Additionally, EDS (Energy-dispersive X-ray spectroscopy) technique was used in order to measure the superficial atomic composition of the samples as chemical changes could occur during or after laser interaction.

2.4.2. Optical characterization

The effect of the fabricated samples on the incident light was measured with a polarimeter (Thorlabs PAX1000IR1). A He-Ne laser (633 nm wavelength) was directed towards the sample at 5° angle with respect to the normal of the surface. Incident laser polarization was controlled with a half wave plate. To better detect birefringence, polarization of the incident beam was linear with an inclination rotated at 45° with respect to the orientation of LIPSS. The specular reflection of light was analyzed using the polarimeter. This device measures the Stokes parameters of the light beam. The Stokes vector is formed by its four components: I, Q, U, and V, which completely define the polarization state of a light beam. I is the intensity of the light beam, Q is the linear component at 0 and 90 degrees, U is linear component at ±45 degrees, and V is the circular component (clock-wise and counter-clockwise). From the Stokes components, the parameters which define the polarization ellipse, that is, the ellipticity and the azimuth, can be easily obtained [34]. Among them, the ellipticity angle describes the circularity of the state, being 0 for linear polarization and ±45° for totally circular polarization. The intermediate values correspond to elliptical states, and the sign of this parameter corresponds to the rotation direction.

2.5. Numerical methods

We have also analyzed the polarization properties of the wave reflected by this type of SWG from a numerical point of view. This allows checking the validity of the assumptions and the experimental results. We have used Rigorous Coupled Wave Analysis (RCWA) method [35–38], also commonly referred as Fourier modal method (FMM) [39] in order to obtain the electric field reflected by the LIPSS on metallic surfaces. In particular, we have used the S^4 implementation [40].

RCWA algorithm divides the profile in layers, as shown in Fig. 2a). We have used a 2D RCWA unit cell to approximate the SWG. In order to simulate the shape of the ripples, we have provided a general definition of the profile as

$$h(x) = A\left\{1 - 2\left[\frac{1 + \cos(2\pi x/p)}{2}\right]^{\beta}\right\}$$

where A is the amplitude of the profile, p is the average period, and β is the fill factor. Except for $\beta = 1$, the profile $h(x)$ is not symmetrical between the upper and the lower parts. In any case, it ranges from $-A$

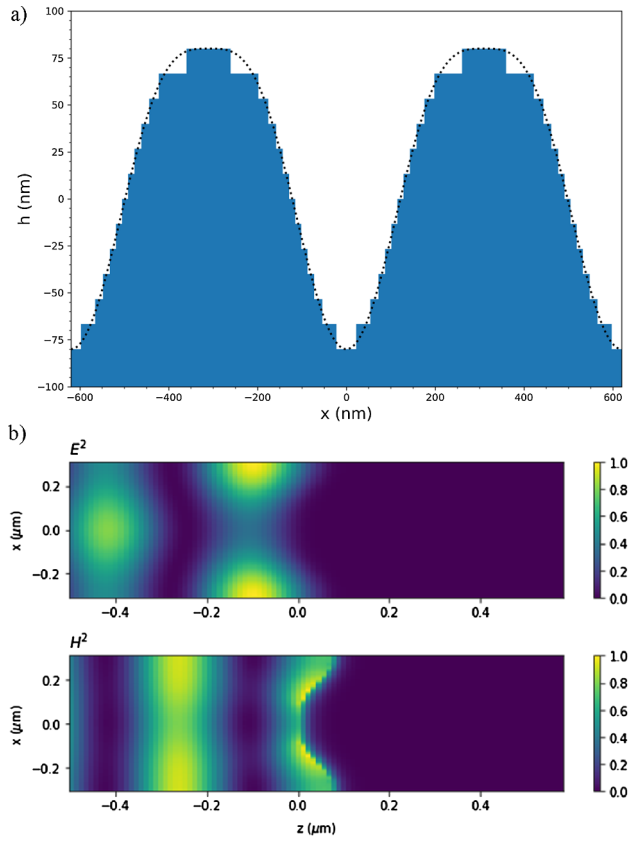

Fig. 2. (a) Profile function (dotted line) and sliced profile (filled space) of the grating with $p = 620$ nm, $A = 80$ nm, $\beta = 1.7$ and number of layers N = 13. (b) Calculated reflected electric (above) and magnetic (below) fields of the same grating illuminated at 633 nm.

to A, and the height of the profile is $2A$.

The illumination is modelled as a plane wave in normal incidence of wavelength 633 nm, as used in the experimental setup (Section 2.4.2), and whose polarization is linear with 45° with respect the axis of the SWG. Experimentally, the incidence angle is 5°, but as it is a low angle, we neglect it for simplicity. The refraction index of the bulk material at this wavelength was measured using spectroscopic ellipsometry, obtaining the complex refraction index $n = 2.3401 + 3.3170i$ at the illumination wavelength. The number of layers in the simulation of the LIPSS profile is N = 13, and the maximum number of orders in the Fourier expansion is G = 51.

As an example, Fig. 2b shows the electric and magnetic reflected fields for a period of $p = 620$ nm. Since the period of the grating is smaller than the incident wavelength, the reflected field is a zero-th order plane wave. Then, the Stokes parameters are computed from the electric field, from which the azimuth and ellipticity angle are calculated.

3. Results

3.1. LIPSS morphology

A study of the LIPSS morphology was performed. Fig. 3 depicts a comparison between a FIB (a) and an AFM profile (b). Similar structures and heights are observed between the two methods. According to the method explained in the previous section, the mean height and standard deviation have been measured for the samples studied and represented in Fig. 5. Results show that LIPSS height is very similar in all the range of studied processing speeds (0.8–2.4 mm/s). The studied samples show heights of around 125 nm with a large dispersion due to irregularities, as represented by the standard deviation. This value for the mean height is in the range of those reported by other groups for steel [41].

Fig. 4 shows a comparison between SEM images of three samples, corresponding to processing speeds of 0.8 mm/s (a), 1.6 mm/s (b) and 2.4 mm/s (c), therefore representing the range of processing speeds used. A notorious feature in the shape of the LIPSS can be seen in Fig. 4a, where the ripples show imperfections along the crest. The same effect has been reported in the literature, which is caused by a higher accumulated fluence [41,42]. On the other hand, Fig. 4c shows LIPSS that in some regions fade, indicating that their structure is not as well defined as in the other cases. The 2D-FFT images shown in the inset of Fig. 4 show two main peaks to the left and right of the origin (in the center of the image). Since the resulting LIPSS are not parallel and uniform structures, the 2D-FFT results show diffused shapes instead of single points, which would correspond to a single frequency and orientation. Instead, there is a stronger peak (with a sickle moon shape) corresponding to the fundamental frequency of the LIPSS and a weaker one (more rounded) at a double frequency, both with some range of frequencies and orientations that vary between samples.

Even though these changes are not evident in the SEM micrographs or in their FFT counterparts, they become more visible in Fig. 4d. This figure shows the ratio between the maximum intensity of the double and fundamental frequency peaks of the LIPSS. It can be seen that this ratio decreases as the processing speed increases. This trend confirms that, as the number of overlapped pulses increases, the shape of the LIPSS changes progressively as mentioned in the description of Fig. 4.

As stated earlier, measuring the distance from the point of maximum intensity to the origin in the 2D-FFT images gives the main frequency or, equivalently, the period of the LIPSS. Additionally, one can measure the frequencies at half-maximum intensity of the transversal profile given by the sickle moon shape. This gives the period dispersion found in Fig. 4e). In this plot, we observe an increase in the range of periods as processing speed increases, giving a wide distribution of LIPSS periods.

The relation between period and processing speed can be seen in Fig. 5. The period of the generated LIPSS increases linearly with the processing speed, from 602 to 651 nm, allowing the classification of these LIPSS as LSFL. A similar behavior and values for a laser emitting at 800 nm have been reported in bibliography [43,44].

Metal oxidation after LIPSS processing is usually not studied or reported. However, in optical applications, and specifically in SWG, it is to expect an influence of the refractive index of the material [45]. Additionally, changes in the refractive index of other materials with different degrees of oxidation have been reported [46]. In this work, we used EDS to analyze our processed samples under different conditions. Results show that the samples have a composition matching that of the stainless steel used, with atomic oxygen present in the processed areas of the samples (Fig. 6). While unprocessed stainless steel shows absence of oxygen, a composition of 1.8% oxygen in mass is found in the samples processed at a speed of 2.2 mm/s. As the processing speed decreases, this percentage increases up to 3% at 1 mm/s.

Therefore, processing speed has a direct effect on the oxygen presence, and we expect it to further increase at lower speeds and decrease at higher speeds. Further studies on this matter should be addressed, since it could provide valuable information for this or other (such as tribological) applications [47].

3.2. Effect of nanostructures on the incident light

Polarimetry results show that the ellipticity of the beam polarization can be modified by varying the processing speed (Fig. 7). As processing speed increases from 0.8 mm/s to 1.6 mm/s, ellipticity angle also increases from 2.91° to 11.04°. However, as the speed further increases, the ellipticity angle starts to decrease again down to 1.18° at a speed of 2.4 mm/s. Therefore, a change in the polarization is observed from

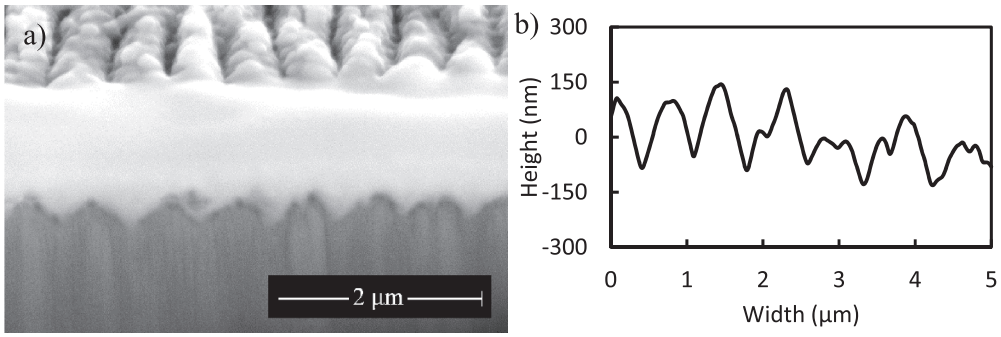

Fig. 3. (a) FIB section, where the profile of the LIPSS can be seen in the interface between light grey (corresponding to a platinum covering used in the process) and dark grey (corresponding to the sample). (b) AFM profile of a sample processed at 0.8 mm/s. Grooves with approximately triangular shape appear on the left area of both images, while on the right half, structures with double peaks arise. The AFM profile looks sharper because of different proportions in the vertical axis.

linear to elliptical with a varying degree of ellipticity, which can be controlled through processing parameters.

At the same time, an effect on the reflectivity can be observed. The reflectivity has been normalized taking as reference the reflectivity of a sample of stainless steel prior to any laser processing, which is 38% of the incident light. As shown in Fig. 7, it increases continuously from 5.8% at 0.8 mm/s to 34% at 2.4 mm/s, with a value of 17.2% at the maximum ellipticity angle.

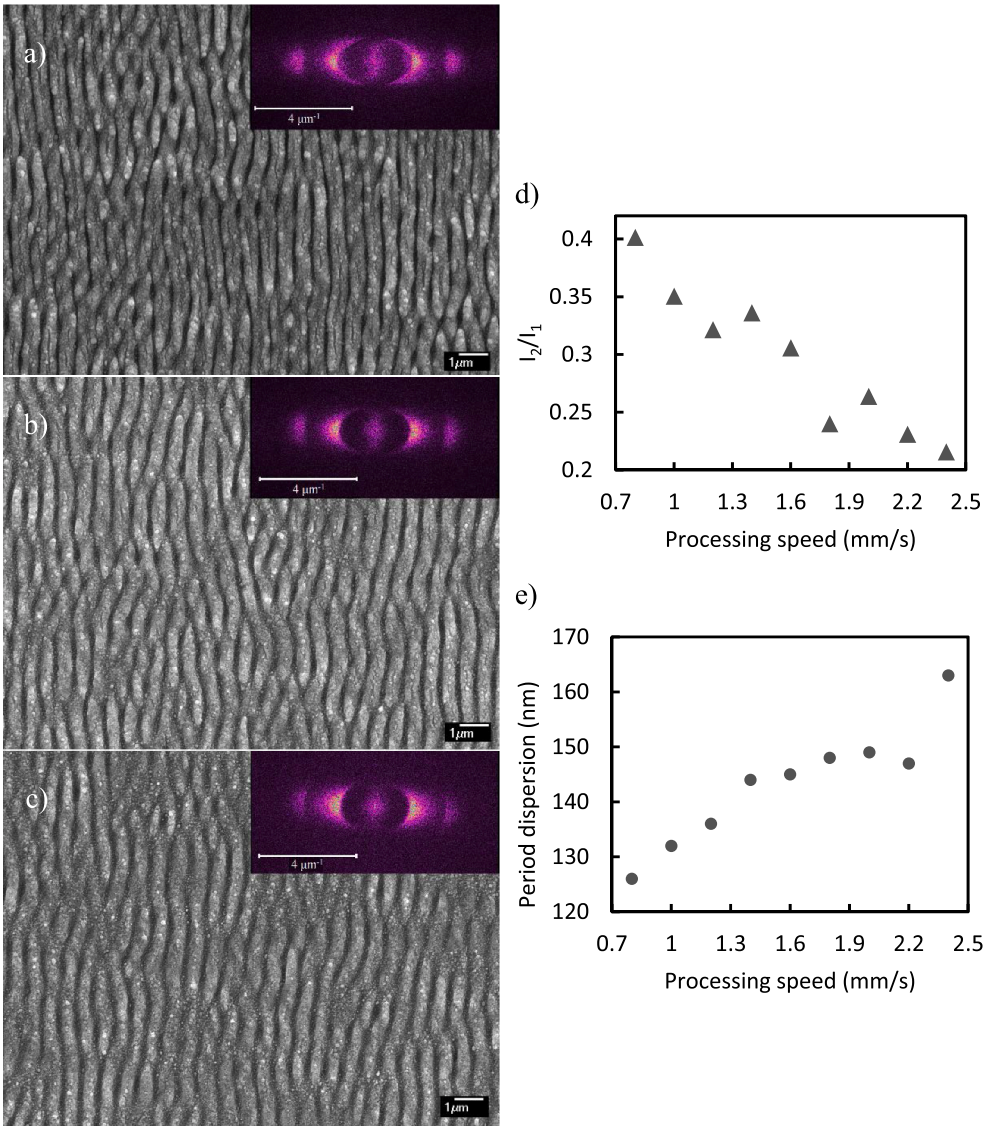

Fig. 4. SEM images of the samples fabricated at (a) 0.8 mm/s, (b) 1.6 mm/s and (c) 2.4 mm/s. Insets: 2D-FFT of the samples. (d) Ratio between intensity of harmonic (I2) and fundamental (I1) frequency of LIPSS as measured in FFT images versus processing speed. (e) FWHM of the period distribution obtained from the 2D-FFT profile.

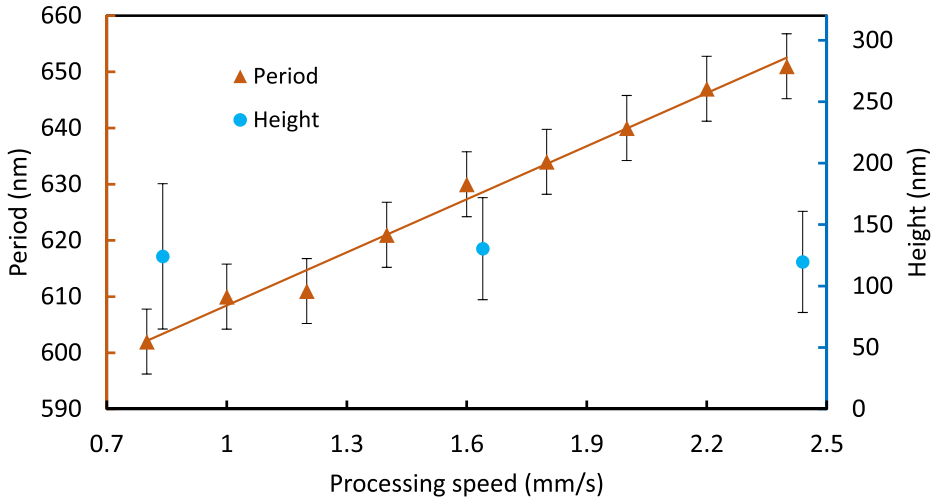

Fig. 5. Period (left axis, orange triangles) and height (right axis, blue circles, with a small offset) of the generated LIPSS versus processing speed of the samples. For the period, a linear fit with R2 = 0.989 and slope 31.5 nm/(mm/s) is found in the studied range.

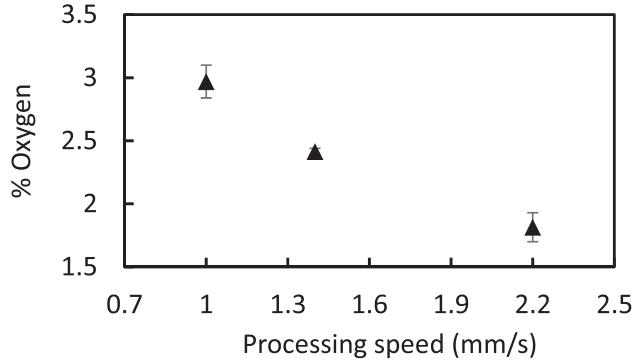

Fig. 6. Oxygen presence in the processed samples versus processing speed.

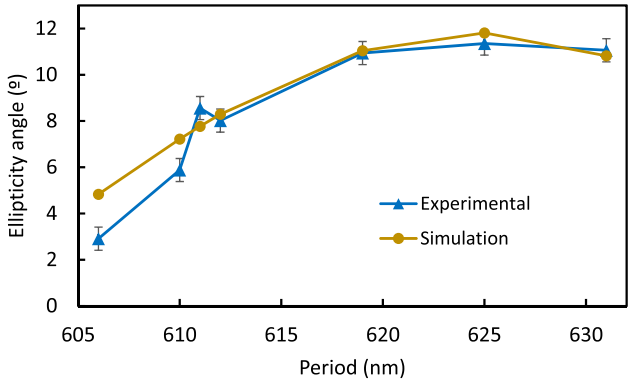

Fig. 8. Comparison between experimental (blue triangles) and calculated (yellow circles) ellipticity angle for periods under the wavelength used in the measurement (633 nm). (For interpretation of the references to colour in this figure legend, the reader is referred to the web version of this article.)

3.3. Optical modeling

In order to validate the experimental data, we have varied the parameters of the profile function in Section 2.5. We have found that the best fitting parameters for the experimental data are $A = 80$ nm and $\beta = 1.7$. Therefore, the height obtained in the simulations, $h = 160$ nm, is in accordance to the experimental results obtained in Fig. 5. Fig. 8 shows the comparison between the experimental values and the numerical calculations performed with the mentioned parameters. The model reproduces the trend and experimental values. Therefore, the height, average shape and periodicity used in the simulation is a good regular equivalent of the irregular surface found experimentally. Even though other combinations of shapes with similar results could in theory be possible, we have not found any other that yields a fitting as good as the one shown in Fig. 8.

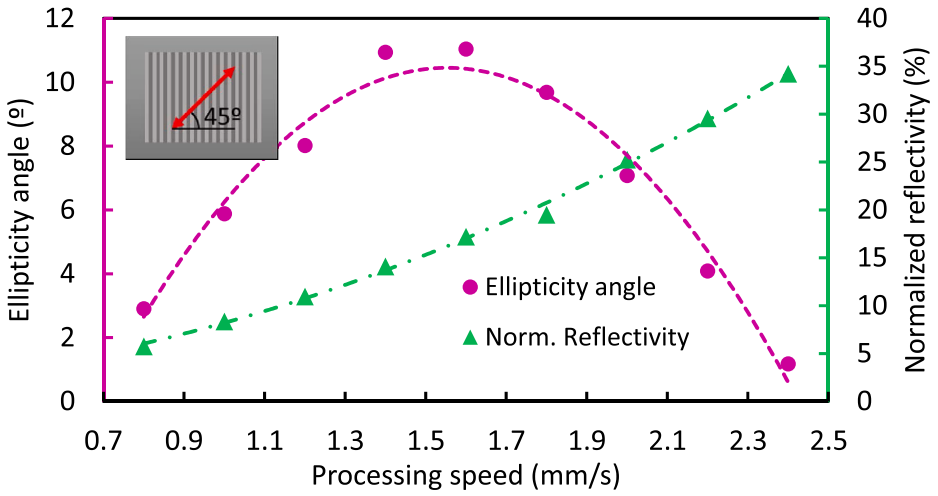

Fig. 7. Ellipticity angle of the reflected light (magenta circles, left axis) and normalized reflectivity (green triangles, right axis) versus processing speed of the samples. The dashed lines are a guide to the eye. Inset: state of polarization of the incident light with respect to the orientation of the LIPSS in the measurements. (For interpretation of the references to colour in this figure legend, the reader is referred to the web version of this article.)

4. Discussion

The coherence in the results between samples suggests that the setup used in this work allows for a consistent fabrication where the parameters are kept constant, specially the spot size. Unlike other processing setups that use microscope objectives with working distances of a few millimeters, our setup uses long focal lenses and therefore has long Rayleigh length, which helps in the positioning of the sample in the Z axis.

In addition, the combination of lenses used in this experiment allows a simpler processing strategy. Since the projected line on the sample is long enough to cover one of the axes, the samples only need to be translated along the axis perpendicular to this line. The required time for the processing of the sample is therefore greatly reduced, and it is especially useful in roll-to-roll processes.

The observed behavior of the samples concerning change in polarization is in agreement with subwavelength gratings causing phase retardation [9,45], so our conclusion is that these properties must be caused by the LIPSS, with their geometry or composition being the key factor to their specific optical behavior.

Since we do not appreciate changes in height in the studied range (Fig. 5), it is reasonable to assume that height is not a factor that influences the changes in the optical behavior of our samples. Similarly, the low oxidation and small variation found in these samples (Fig. 6) suggest that oxygen concentration is not the main cause of the decrease in reflectance at lower speeds.

On the other hand, we see a clear trend in LIPSS period (Fig. 5), which could be the main cause of the change in behavior for the different samples. Although a higher reflectivity and a greater change in polarization from linear to elliptical can be achieved, we believe that this effect is limited by the great distribution observed in periods and heights (Figs. 4e and 5, respectively), making the surface irregular and this way reducing its effect as a single grating. In addition to this, the decrease in reflectivity at lower fabrication speeds (Fig. 7) could be related to the increase in the presence of double frequency LIPSS as seen in Fig. 4d.

Additionally, the numerical simulations with RCWA show that the shape of the LIPSS can be approximated to a periodic function that alleviates the computational requirements of the simulation and provides a simplified approximation. This method has been used to find an effective height and shape of the generated nanostructures. The shape found is, in general, consistent with the shape of the LIPSS observed, since it conserves the conical shape. The effective height found in the simulations is 160 nm, which is just within the values of heights extracted from AFM measurements (around 125 ± 45 nm), although far from the average height. This suggest either that AFM measurements are not reaching the bottom of the valleys formed by LIPSS or that not all heights influence the ellipticity measurements equally. Since the shape of LIPSS changes slightly between samples, this could also be a factor to take into account in the model. In any case, we see from the simulations that the change in periodicity does indeed change the ellipticity in a way similar to what we have observed experimentally, supporting our hypothesis.

To sum up, we believe that the period of the LIPSS is the key factor that alters the behavior of our polarization gratings, with some influence from their structuration (distribution of periods) that mainly affects their reflectivity. By changing the processing parameters, we can control these factors, as shown in this work, and therefore tailor the properties of the resulting polarization grating. Other factors could be studied as well, such as changes in height, which is another property of polarization gratings that influence the polarization change [45].

Improving this fabrication method in order to achieve higher reflectivity and specific changes in polarization would enable the use of these devices as reflective waveplates. The main advantage for this type of waveplates is that the fabrication method is a one-step and very fast process that it is not restricted by the type of substrate material, demanding processing conditions or over-expensive equipment.

5. Conclusions

In this work, we have proven the fast fabrication of LIPSS on stainless steel with a setup based on cylindrical lens that projects a line of dimensions 32 μm by 6 mm (half-widths at e^{-2}), covering a large area with only a one-dimensional scan at speeds in the order of 1 mm/s. This setup allows a stable and replicable fabrication and shows their potential application as reflective waveplates, replacing other complex, demanding and polluting methods. The readily use of these devices in applications depends on the particular demands of each application. For example, the mentioned application as reflective waveplates would require very high reflectivity (>90%) and a fixed amount of polarization change, such as achieving complete circular polarization (45° in ellipticity angle). Although the potential of this technique to fabricate reflective waveplates has been demonstrated, using these devices in real life operation requires further improvements.

As mentioned, the maximum values for change in ellipticity angle and reflectivity reported here are not optimal. However, our findings suggest that better values could be obtained by achieving LIPSS with better quality (less periodic or angular dispersion) or by applying a coating on the processed sample that would attenuate irregularities. We strongly believe that through these improvements real operational waveplates can be fabricated, and therefore future work will focus on these topics.

However, other applications requiring the detection of a change in polarization, such as optical codification of phase shift detection would be readily usable with the current fabrication process depending on the sensibility of the detector.

We have studied the morphology of the LIPSS and performed numerical simulations. Our results show that, although the exact relation between polarization change and LIPSS morphology is complex due to the variety of factors in play (profile shape, period, irregularities, oxide formation or other compositional changes), two are the main factors that influence this change: period and LIPSS regularity. Since both factors can be controlled adjusting laser parameters, the amount of induced polarization change can be tailored in the fabrication process.

CRediT authorship contribution statement

A. San-Blas: Investigation, Conceptualization, Methodology, Validation, Writing - original draft, Visualization. **M. Martinez-Calderon:** Methodology, Writing - original draft, Writing - review & editing. **J. Buencuerpo:** Software, Formal analysis, Writing - review & editing. **L.M. Sanchez-Brea:** Software, Validation, Writing - review & editing, Visualization. **J. del Hoyo:** Software, Formal analysis, Validation, Writing - review & editing. **M. Gómez-Aranzadi:** Writing - review & editing, Supervision. **A. Rodríguez:** Writing - review & editing, Supervision. **S.M. Olaizola:** Conceptualization, Methodology, Writing - review & editing, Project administration, Funding acquisition.

Declaration of Competing Interest

The authors declare that they have no known competing financial interests or personal relationships that could have appeared to influence the work reported in this paper.

Acknowledgments

Ministerio de Economía y Competitividad (MINECO) “Ecograb” of “Programa Estatal de Investigacion, Desarrollo e Innovacion Orientada a los Retos de la Sociedad” (RTC-2016-5277-5); co-financed with structural funds of the European Union.

LASER4SURF has received funding from the European Union’s Horizon 2020 research and innovation programme under grant agreement No. 768636.

References

[1] N. Bonod, J. Neauport, Diffraction gratings: from principles to applications in high-intensity lasers, Adv. Opt. Photon. 8 (2016) 156–199, https://doi.org/10.1364/AOP.8.000156.

[2] R.J. King, Quarter-wave retardation systems based on the Fresnel rhomb principle, J. Sci. Instrum. 43 (1966).

[3] J. Haberko, P. Wasylczyk, Reflecting metallic metasurfaces designed with stochastic optimization as waveplates for manipulating light polarization, Opt. Commun. 410 (2018) 740–743, https://doi.org/10.1016/j.optcom.2017.11.044.

[4] R.-C. Tyan, A.A. Salvekar, H.-P. Chou, C.-C. Cheng, A. Scherer, P.-C. Sun, F. Xu, Y. Fainman, Design, fabrication, and characterization of form-birefringent multilayer polarizing beam splitter, J. Opt. Soc. Am. A 14 (1997) 1627–1636, https://doi.org/10.1364/JOSAA.14.001627.

[5] X. Zheng, W. Smith, J. Jackson, B. Moran, H. Cui, D. Chen, J. Ye, N. Fang, N. Rodriguez, T. Weisgraber, C.M. Spadaccini, Multiscale metallic metamaterials, Nat. Mater. 15 (2016) 1100–1106, https://doi.org/10.1038/nmat4694.

[6] S.L. Wadsworth, G.D. Boreman, Broadband infrared meanderline reflective quarter-wave plate, Opt. Express 19 (2011) 10604–10612, https://doi.org/10.1364/OE.19.010604.

[7] B. Aurand, C. Rdel, H. Zhao, S. Kuschel, M. Wnsche, O. Jckel, M. Heyer, F. Wunderlich, M.C. Kaluza, G.G. Paulus, T. Kuehl, Note: a large aperture four-mirror reflective wave-plate for high-intensity short-pulse laser experiments, Rev. Sci. Instrum. 83 (2012) 2012–2015, https://doi.org/10.1063/1.3694659.

[8] S. Pan, L. Tan, H.S. Kwok, Broadband reflective polarizers based on form birefringence for ultra-thin liquid crystal displays, Opt. Express 25 (2017) 17499, https://doi.org/10.1364/oe.25.017499.

[9] I. Yamada, T. Ishihara, J. Yanagisawa, Reflective waveplate with subwavelength grating structure, Jpn. J. Appl. Phys. 54 (2015), https://doi.org/10.7567/JJAP.54.092203.

[10] M. Suzuki, A. Takada, T. Yamada, T. Hayasaka, K. Sasaki, E. Takahashi, S. Kumagai, Antireflection coatings with FeSi2 layer: application to low-reflectivity wire grid polarizers, Thin Solid Films 519 (2011) 8485–8489, https://doi.org/10.1016/j.tsf.2011.05.023.

[11] H. Kikuta, Y. Ohira, K. Iwata, Achromatic quarter-wave plates using the dispersion of form birefringence, Appl. Opt. 36 (1997) 1566, https://doi.org/10.1364/ao.36.001566.

[12] A. Emoto, M. Nishi, M. Okada, S. Manabe, S. Matsui, N. Kawatsuki, H. Ono, Form birefringence in intrinsic birefringent media possessing a subwavelength structure, Appl. Opt. 49 (2010) 4355–4361, https://doi.org/10.1364/AO.49.004355.

[13] M. Born, E. Wolf, E. Hecht, Principles of optics: electromagnetic theory of propagation, interference and diffraction of light, Phys. Today 53 (2000) 77–78, https://doi.org/10.1063/1.1325200.

[14] S.S. Stafeev, V.V. Kotlyar, A.G. Nalimov, M.V. Kotlyar, L. O'Faolain, Subwavelength gratings for polarization conversion and focusing of laser light, Photon. Nanostruct. – Fundam. Appl. 27 (2017) 32–41, https://doi.org/10.1016/j.photonics.2017.09.001.

[15] S.S. Stafeev, M.V. Kotlyar, L. O'Faolain, A.G. Nalimov, V.V. Kotlyar, Subwavelength gratings for generating azimuthally polarized beams, CEUR Workshop Proc. (2016) 125–131, https://doi.org/10.18287/1613-0073-2016-1638-125-131.

[16] Z. Ghadyani, I. Vartiainen, I. Harder, W. Iff, A. Berger, N. Lindlein, M. Kuittinen, Concentric ring metal grating for generating radially polarized light, Appl. Opt. 50 (2011) 2451–2457, https://doi.org/10.1364/AO.50.002451.

[17] N. Yu, F. Aieta, P. Genevet, M.A. Kats, Z. Gaburro, F. Capasso, A broadband, background-free quarter-wave plate based on plasmonic metasurfaces, Nano Lett. 12 (2012) 6328–6333, https://doi.org/10.1021/nl303445u.

[18] S.S. Stafeev, A.G. Nalimov, M.V. Kotlyar, D. Gibson, S. Song, L. O'Faolain, V.V. Kotlyar, Microlens-aided focusing of linearly and azimuthally polarized laser light, Opt. Express 24 (2016) 29800, https://doi.org/10.1364/oe.24.029800.

[19] A. Kravchenko, A. Shevchenko, V. Ovchinnikov, P. Grahn, M. Kaivola, Fabrication and characterization of a large-area metal nano-grid wave plate, Appl. Phys. Lett. 103 (2013) 33111, https://doi.org/10.1063/1.4813756.

[20] H.M. Phillips, D.L. Callahan, R. Sauerbrey, G. Szabó, Z. Bor, Sub-100 nm lines produced by direct laser ablation in polyimide, Appl. Phys. Lett. 58 (1991) 2761–2763, https://doi.org/10.1063/1.104778.

[21] E. Stankevičius, M. Gedvilas, B. Voisiat, M. Malinauskas, G. Račiukaitis, Fabrication of periodic micro-structures by holographic lithography, Lith. J. Phys. 53 (2013) 227–237, https://doi.org/10.3952/physics.v53i4.2765.

[22] M. Bieda, M. Siebold, A.F. Lasagni, Fabrication of sub-micron surface structures on copper, stainless steel and titanium using picosecond laser interference patterning, Appl. Surf. Sci. 387 (2016) 175–182, https://doi.org/10.1016/j.apsusc.2016.06.100.

[23] M. Birnbaum, Semiconductor surface damage produced by ruby lasers, J. Appl. Phys. 36 (1965) 3688–3689, https://doi.org/10.1063/1.1703071.

[24] J. Bonse, S. Hohm, S.V. Kirner, A. Rosenfeld, J. Kruger, Laser-induced periodic surface structures - a scientific evergreen, IEEE J. Sel. Top. Quantum Electron. 23 (2017), https://doi.org/10.1109/JSTQE.2016.2614183.

[25] A. Pan, A. Dias, M. Gomez-Aranzadi, S.M. Olaizola, A. Rodriguez, Formation of laser-induced periodic surface structures on niobium by femtosecond laser irradiation, J. Appl. Phys. 115 (2014), https://doi.org/10.1063/1.4873459.

[26] E. Granados, M. Martinez-Calderon, M. Gomez, A. Rodriguez, S.M. Olaizola, Photonic structures in diamond based on femtosecond UV laser induced periodic surface structuring (LIPSS), Opt. Express 25 (2017) 15330, https://doi.org/10.1364/oe.25.015330.

[27] M. Martínez-Calderon, M. Manso-Silván, A. Rodríguez, M. Gómez-Aranzadi, J.P. García-Ruiz, S.M. Olaizola, R.J. Martín-Palma, Surface micro- and nano-texturing of stainless steel by femtosecond laser for the control of cell migration, Sci. Rep. 6 (2016) 1–10, https://doi.org/10.1038/srep36296.

[28] F. Courvoisier, J. Zhang, M.K. Bhuyan, M. Jacquot, J.M. Dudley, Applications of femtosecond Bessel beams to laser ablation, Appl. Phys. A 112 (2013) 29–34, https://doi.org/10.1007/s00339-012-7201-2.

[29] M.S. Sidhu, P. Munjal, K.P. Singh, High-fidelity large area nano-patterning of silicon with femtosecond light sheet, Appl. Phys. A Mater. Sci. Process. 124 (2018) 1–5, https://doi.org/10.1007/s00339-017-1459-3.

[30] L. Yang, A. El-Tamer, U. Hinze, J. Li, Y. Hu, W. Huang, J. Chu, B.N. Chichkov, Parallel direct laser writing of micro-optical and photonic structures using spatial light modulator, Opt. Lasers Eng. 70 (2015) 26–32, https://doi.org/10.1016/j.optlaseng.2015.02.006.

[31] S.K. Das, K. Dasari, A. Rosenfeld, R. Grunwald, Extended-area nanostructuring of TiO2 with femtosecond laser pulses at 400nm using a line focus, Nanotechnology. 21 (2010), https://doi.org/10.1088/0957-4484/21/15/155302.

[32] M. Ardron, N. Weston, D. Hand, A practical technique for the generation of highly uniform LIPSS, Appl. Surf. Sci. 313 (2014) 123–131, https://doi.org/10.1016/j.apsusc.2014.05.154.

[33] Y. Jin, O.J. Allegre, W. Perrie, K. Abrams, J. Ouyang, E. Fearon, S.P. Edwardson, G. Dearden, Dynamic modulation of spatially structured polarization fields for real-time control of ultrafast laser-material interactions, Opt. Express 21 (2013) 25333, https://doi.org/10.1364/oe.21.025333.

[34] D.H. Goldstein, Polarized Light, third ed., 2017. https://doi.org/10.1201/b10436.

[35] P. Lalanne, G.M. Morris, Highly improved convergence of the coupled-wave method for TM polarization, J. Opt. Soc. Am. A: 13 (1996) 779–784, https://doi.org/10.1364/JOSAA.13.000779.

[36] M.G. Moharam, E.B. Grann, D.A. Pommet, T.K. Gaylord, Formulation for stable and efficient implementation of the rigorous coupled-wave analysis of binary gratings, J. Opt. Soc. Am. A: 12 (1995) 1068–1076, https://doi.org/10.1364/JOSAA.12.001068.

[37] M.G. Moharam, T.K. Gaylord, Diffraction analysis of dielectric surface-relief gratings, J. Opt. Soc. Am. 72 (1982) 1385–1392, https://doi.org/10.1364/JOSA.72.001385.

[38] M.G. Moharam, T.K. Gaylord, Rigorous coupled-wave analysis of planar-grating diffraction, J. Opt. Soc. Am. 71 (1981) 811–818, https://doi.org/10.1364/JOSA.71.000811.

[39] L. Li, New formulation of the Fourier modal method for crossed surface-relief gratings, J. Opt. Soc. Am. A: 14 (1997) 2758–2767, https://doi.org/10.1364/JOSAA.14.002758.

[40] V. Liu, S. Fan, S^4: A free electromagnetic solver for layered periodic structures, Comput. Phys. Commun. 183 (2012) 2233–2244, https://doi.org/10.1016/j.cpc.2012.04.026.

[41] J. Yao, C. Zhang, H. Liu, Q. Dai, L. Wu, S. Lan, A.V. Gopal, V.A. Trofimov, T.M. Lysak, Selective appearance of several laser-induced periodic surface structure patterns on a metal surface using structural colors produced by femtosecond laser pulses, Appl. Surf. Sci. 258 (2012) 7625–7632, https://doi.org/10.1016/j.apsusc.2012.04.105.

[42] A. Ruiz de la Cruz, R. Lahoz, J. Siegel, G.F. de la Fuente, J. Solis, High speed inscription of uniform, large-area laser-induced periodic surface structures in Cr films using a high repetition rate fs laser, Opt. Lett. 39 (2014) 2491, https://doi.org/10.1364/ol.39.002491.

[43] I. Gnilitskyi, T.J.Y. Derrien, Y. Levy, N.M. Bulgakova, T. Mocek, L. Orazi, High-speed manufacturing of highly regular femtosecond laser-induced periodic surface structures: physical origin of regularity, Sci. Rep. 7 (2017) 1–11, https://doi.org/10.1038/s41598-017-08788-z.

[44] G. Li, J. Li, Y. Hu, C. Zhang, X. Li, J. Chu, W. Huang, Femtosecond laser color marking stainless steel surface with different wavelengths, Appl. Phys. A Mater. Sci. Process. 118 (2014) 1189–1196, https://doi.org/10.1007/s00339-014-8868-3.

[45] Y. Pang, R. Gordon, Metal nano-grid reflective wave plate, Opt. Express 17 (2009) 2871, https://doi.org/10.1364/oe.17.002871.

[46] E.V. Astrova, V.A. Tolmachev, Effective refractive index and composition of oxidized porous silicon films, Mater. Sci. Eng., B 69–70 (2000) 142–148, https://doi.org/10.1016/S0921-5107(99)00236-6.

[47] J. Bonse, S.V. Kirner, M. Griepentrog, D. Spaltmann, J. Krüger, Femtosecond laser texturing of surfaces for tribological applications, Materials (Basel) 11 (2018) 1–19, https://doi.org/10.3390/ma11050801.